Magnetic excitation and local magnetic susceptibility of the excitonic insulator Ta_2NiSe_5 investigated by ^{77}Se NMR

Shang Li, Shunsuke Kawai, Yoshiaki Kobayashi, and Masayuki Itoh
Department of Physics, Graduate School of Science, Nagoya University, Furo-cho, Chikusa-ku, Nagoya 464-8602, Japan

(Received 30 November 2017; revised manuscript received 9 March 2018; published 17 April 2018)

^{77}Se NMR measurements were made on polycrystalline and single-crystalline samples to elucidate local magnetic susceptibility and magnetic excitation of Ta_2NiSe_5, which is proposed to undergo an exciton condensation accompanied by a structural transition at $T_c = 328$ K. We determine the ^{77}Se Knight shift tensors for the three Se sites and analyze their anisotropy based on the site symmetry. The temperature dependence of the Knight shift is discussed on the basis of spin and orbital susceptibilities calculated for two-chain and two-dimensional three-band models. The large fraction of the Se $4p$ orbital polarization due to the mixing between Ni $3d$ and Se $4p$ orbitals is estimated from the analysis of the transferred hyperfine coupling constant. Also the nuclear spin-lattice relaxation rate $1/T_1$ is found not to show a coherent peak just below T_c and to obey the thermally activated temperature dependence with a spin gap energy of 1770 ± 40 K. This behavior of $1/T_1$ monitors the exciton condensation as proposed by the theoretical study of $1/T_1$ based on the three-chain Hubbard model for the excitonic insulator.

DOI: 10.1103/PhysRevB.97.165127

I. INTRODUCTION

The excitonic insulator has an exotic electronic state that appears in semiconductors and semimetals [1–5]. An electron-hole pair called an exciton is formed by the strong Coulomb interaction if the binding energy of the electron-hole pair is much higher than the gap energy between the valence-band top and conduction-band bottom for semiconductors or the overlapping energy for semimetals. Then the BCS or Bose-Einstein condensation takes place in the semimetals or semiconductors, leading to the excitonic insulator. A few materials, $TmSe_{1-x}Te_x$ [6–8], CaB_6 [9–11], and $1T$-$TiSe_2$ [12–14], were discussed as candidates for the excitonic insulator. Recently, Ta_2NiSe_5 was proposed as a new candidate from an angle-resolved photoemission spectroscopy (ARPES) study [15,16].

Ta_2NiSe_5 crystallizes into the monoclinic structure (space group $C2/c$) at room temperature [17]. It has a three-chain structure in which $NiSe_4$ tetrahedra form one chain and $TaSe_6$ octahedra form two chains along the a axis as a unit structure, as shown in Fig. 1. These chains form a layer along the c axis, and the layers are weakly coupled via the van der Waals interaction. Electrical resistivity shows quasi-one-dimensional (quasi-1D) metallic behavior above ~550 K and a reversible change in slope at $T_c = 328$ K, where a structural transition from the high-T orthorhombic to low-T monoclinic phases takes place [18]. Magnetic susceptibility is diamagnetic in the measured T range below 900 K and shows a drop at T_c and a rapid increase due to an impurity below ~100 K [18]. Recently, Ta_2NiSe_5 was proposed as a candidate for the excitonic insulator, which is stabilized below T_c, on the basis of a flat Ni $3d$-Se $4p$ valance band observed by ARPES experiments [15,16]. This band structure was reproduced by first-principles calculation by Kaneko *et al.*, who also discussed the excitonic insulator transition based on the three-chain model composed of one Ni-Se and two Ta chains [19–22]. After the ARPES experiments, intensive experimental and theoretical studies were carried out to understand the excitonic state in Ta_2NiSe_5. Lu *et al.* observed an optical excitation gap with $E_{op} \sim 0.16$ eV in a nearly zero gap semiconductor, Ta_2NiSe_5. They also proposed the phase diagram, the transition temperature versus energy gap under chemical pressure due to S doping and physical pressure [23]. At ~3 GPa, a pressure-induced structural transition was reported to take place with coherent sliding between weakly coupled layers [24]. The nonequilibrium dynamics of the electronic structure was investigated by time-resolved photoemission spectroscopy and ARPES [25]. Also an ellipsometric experiment uncovered unusual excitonic resonances [26]. The optical conductivity was observed to have large anisotropic electronic and phononic properties and to show a significant temperature T dependence of the energy gap [27]. Based on the thickness dependence study of Raman spectroscopy, scanning tunneling microscopy, and transport properties, the stabilization of the excitonic insulator phase was discussed to be affected by Coulomb interaction rather than by the electron-phonon interaction [28]. From theoretical considerations, Sugimoto *et al.* showed that the nuclear spin-lattice relaxation rate $1/T_1$ and the ultrasonic attenuation rate are useful for detecting the excitonic insulating state [29]. The formation of the excitonic insulating state was shown to result in the T-dependent diamagnetic orbital susceptibility in a two-dimensional three-band model [30] and a two-chain model [31]. More recently, Fulde-Ferrell-Larkin-Ovchinnikov excitonic orders, which may appear in Ta_2NiSe_5 at high pressure, were also discussed on the basis of the three-chain Hubbard model [32,33].

NMR is a useful probe to study magnetic and electronic properties of a substance from the local point of view. NMR can monitor the intrinsic magnetic susceptibility of Ta_2NiSe_5, which is partly hidden behind the Curie-type magnetic susceptibility due to impurities. Furthermore, $1/T_1$ is expected to

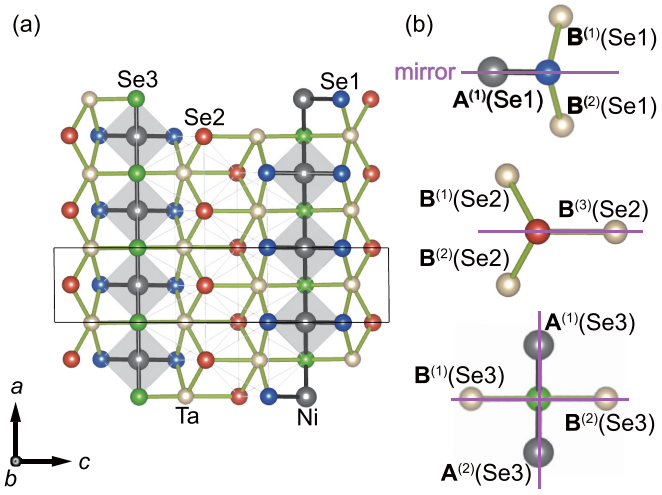

FIG. 1. (a) Crystal structure of Ta_2NiSe_5 viewed from the b axis. (b) Local structures around the Se1, Se2, and Se3 sites. The solid rectangle represents a unit cell. $\mathbf{A}^{(i)}(\mathrm{Se}j)$ and $\mathbf{B}^{(i)}(\mathrm{Se}j)$ ($i = 1, 2$ and $j = 1, 2, 3$) denote the transferred hyperfine coupling tensors at the Sej site coming from the ith Ni and Ta sites, respectively. The purple lines represent mirror planes, on which the Se1-Se3 sites are located, perpendicular to the a or c axis in the orthorhombic phase (space group $Cmcm$ [18]) above $T_c = 328$ K.

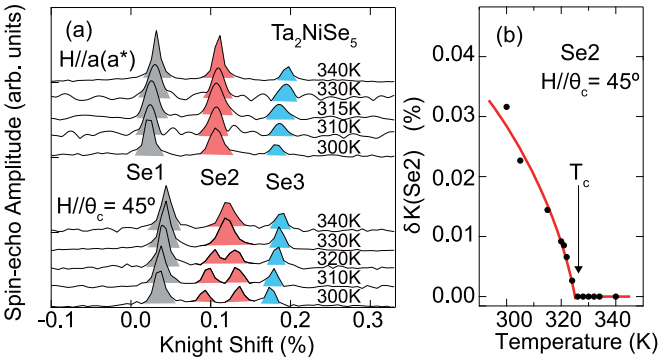

FIG. 2. (a) ^{77}Se NMR spectra around T_c for $H_0 \parallel a^*$ ($H_0 \parallel a$) and $\theta_c = 45°$ in the monoclinic (orthorhombic) phase of the single-crystalline Ta_2NiSe_5 sample. (b) Temperature dependence of the difference between the Knight shifts of the Se2 spectra δK(Se2). The solid curve is a guide to the eye.

directly measure the formation of the excitonic condensation, as discussed by Sugimoto and Ohta [30].

In this study, we have conducted ^{77}Se NMR measurements on polycrystalline and single-crystalline samples to study local magnetic susceptibility and magnetic excitation in Ta_2NiSe_5. We determine the ^{77}Se Knight shift tensors of the Se1–Se3 sites in the monoclinic and orthorhombic phases which are governed by the transferred hyperfine (TH) fields dependent on the local configuration. The Knight shifts are discussed on the basis of spin and orbital susceptibilities calculated in the two-chain and two-dimensional three-band models. Here, $1/T_1$ is found not to show a coherence peak just below T_c, consistent with the result of the BCS-type mean-field calculation for the three-chain Hubbard model with an electron-phonon coupling. Also $1/T_1$ shows the spin-gap behavior with an energy gap of $E_g = 1770$ K in the monoclinic phase.

II. EXPERIMENTAL PROCEDURE

Polycrystalline samples of Ta_2NiSe_5 used in this study were prepared using a solid-state reaction as described in Refs. [17,18]. After appropriate amounts of Ta (99.9%), Ni (99.99%), and Se (99.9%) were mixed and pressed into a pellet, the pellet was heated in an evacuated quartz tube at 850 °C for 100 h with an intermediate reground. On the other hand, single crystals were grown by the chemical-vapor-transport method using I_2 as a transport agent. The elements and I_2 were sealed in an evacuated quartz ampoule and heated in a furnace with a temperature gradient from 960 °C at one end of the ampoule to 830 °C at the other end. The samples were confirmed to have monoclinic structure at room temperature by powder x-ray diffraction.

^{77}Se NMR measurements were performed utilizing a coherent pulsed spectrometer and a superconducting magnet with a constant field of $H_0 = 6.1052$ T. Fourier-transformed (FT) NMR spectra were measured for spin-echo signals. The Knight shift of ^{77}Se nuclei with nuclear spin $I = 1/2$ was determined using $(CH_3)_2Se$ as a reference. A two-axis goniometer was utilized to measure the angular dependence of the NMR spectrum and the Knight shift for the single crystal below 340 K. On the other hand, we used a home-made NMR probe with a high-temperature furnace and a one-axis goniometer for the single crystal above 340 K. Also the powder sample was sealed in an evacuated quartz tube for the high-temperature measurement. The ^{77}Se nuclear spin-lattice relaxation rate $1/T_1$ was measured with the inversion recovery method.

III. EXPERIMENTAL RESULTS

A. NMR spectrum and Knight shift

The single-crystal ^{77}Se NMR spectrum with $H_0 \parallel a^*$ at 300 K in the monoclinic phase is presented in Fig. 2(a), where the a^* axis is introduced as an axis perpendicular to the b and c axes. It should be noted that β_m, the monoclinic angle between the a and c axes, at 300 K is 90.53°, which is very close to 90° [18]. This spectrum is composed of three lines coming from the Se1–Se3 sites, as seen in Fig. 2(a). Among the NMR lines the Se2 one is split into two lines for $H_0 \parallel \theta_c = 45°$, where θ_c is the angle between H_0 and the a^* axis in the a^*b plane. The definitions for θ_{a^*} and θ_b can be obtained by cyclic permutation of a^*, b, and c. The Se2 spectrum for $H_0 \parallel a$ (a^*) shows little change with increasing T across T_c, whereas the Se2 spectrum for $H_0 \parallel \theta_c = 45°$ is composed of two lines below $T_c = 326$ K in this sample, and the difference between the Knight shifts of the two lines δK(Se2) decreases toward T_c and vanishes above T_c, as seen in Fig. 2(b). Thus, the present NMR spectra clearly monitor the structural transition at T_c.

Each line at 300 K in the monoclinic phase shows the angular dependence with H_0 rotated in the a^*b, bc, and ca^* planes, as shown in Figs. 3(a), 3(b) and 3(c), respectively. The site symmetry at the Se1 (Se2) site leads to the line splitting for H_0 in the bc and ca^* (a^*b and bc) planes, whereas Se3 shows no splitting. Each angular dependence of K in the a^*b plane

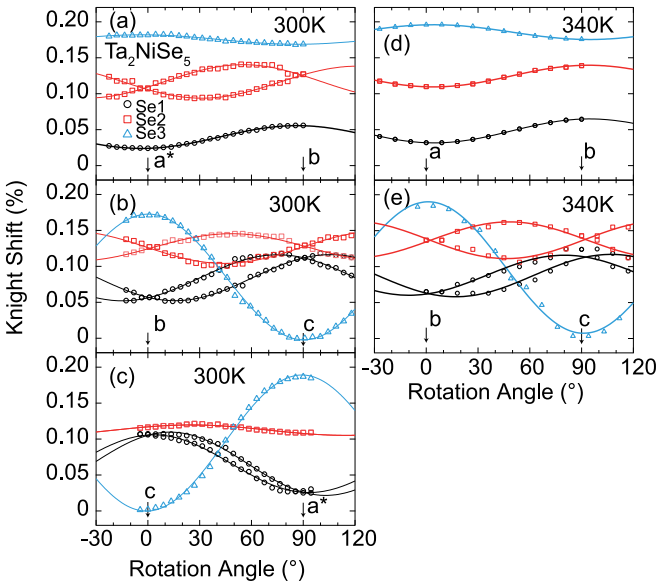

FIG. 3. Angular dependences of the ^{77}Se Knight shifts with H_0 rotated in the (a) a^*b, (b) bc, and (c) ca^* planes at 300 K and in the (d) ab and (e) bc planes at 340 K in the single-crystalline Ta_2NiSe_5 sample. The solid curves are the results of fitting the data to Eq. (1) (see text).

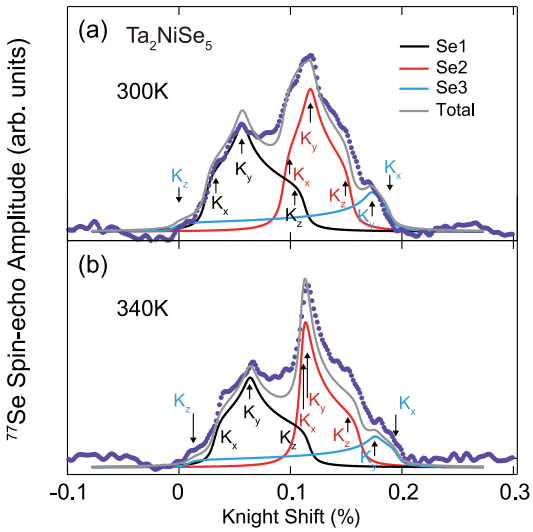

FIG. 4. ^{77}Se NMR spectra at (a) 300 K in the monoclinic phase and at (b) 340 K in the orthorhombic phase of the polycrystalline Ta_2NiSe_5 sample. The solid curves are 3D randomly oriented powder patterns of Se1, Se2, and Se3 calculated for the Knight shifts listed in Table I. The gray curve is the summation of the Se1, Se2, and Se3 powder patterns. The arrows with the symbols K_x, K_y, and K_z represent the singularity positions of the powder pattern and provide the principal values of the Knight shift tensor.

is expressed as

$$K = k_{1,c} + k_{2,c}\cos 2\theta_c + k_{3,c}\sin 2\theta_c, \quad (1)$$

with

$$k_{1,c} = (K_{a^*a^*} + K_{bb})/2, \quad k_{2,c} = (K_{a^*a^*} - K_{bb})/2,$$
$$k_{3,c} = K_{a^*b},$$

where $K_{\alpha\beta}$ (α, $\beta = a^*$, b, and c) are the K tensor components [34,35]. The equations of K in the bc and ca^* planes can be obtained by cyclic permutation of a^*, b, and c. By fitting the experimental data to the equations and diagonalization of the tensors in the a^*bc coordinate system, we can obtain the principal components of the K tensor, K_x, K_y, and K_z, for Se1–Se3 as listed in Table I. The principal axes are tilted from the crystal axes for the Se1 and Se2 sites, whereas the z (x) axis is almost along the c (a^*) axis for the Se3 site. At 340 K in the orthorhombic phase, the angular dependences of K with H_0 rotated in the ab and bc planes are presented in Figs. 3(d) and 3(e). From the same analysis of the K tensors, we also obtain the K_x, K_y, and K_z values at 340 K, as listed in Table I. Here, the site symmetry requires that the a axis is one of the principal axes for the Se1–Se3 sites. Thus, the z axis is parallel to the direction at $\theta_a = \pm 74^\circ$ ($\theta_a = \pm 45^\circ$) in the bc plane for the Se1 (Se2) site, whereas it is along the c axis for the Se3 site.

TABLE I. ^{77}Se Knight shifts, K_x, K_y, and K_z, at 300 K in the monoclinic phase and at 340 K in the orthorhombic phase of Ta_2NiSe_5.

T (K)	Site	K_x (%)	K_y (%)	K_z (%)
300	Se1	0.025	0.056	0.113
	Se2	0.094	0.118	0.154
	Se3	0.189	0.173	−0.003
340	Se1	0.032	0.064	0.117
	Se2	0.110	0.112	0.162
	Se3	0.196	0.176	0.009

These Knight shifts can reproduce the powder ^{77}Se NMR spectra at 300 and 340 K, as presented in Figs. 4(a) and 4(b), respectively. Here, the experimental spectra are compared with the summation of three three-dimensional (3D) randomly oriented powder patterns, Se1–Se3, calculated from the Knight shifts listed in Table I. Each asymmetric powder pattern with a peak for K_y and steps for K_x and K_z is convoluted by a Lorentzian with a full width at half maximum (FWHM) of 3.3 kHz. Also the intensity ratio of the Se1, Se2, and Se3 powder patterns is assumed to be 2:2:1, the number ratio of the Se sites.

B. Temperature dependence of the Knight shift

Figures 5(a), 5(b) and 5(c) show the T dependences of K_a (K_{a^*}), K_b, and K_c for the Se1, Se2, and Se3 sites, respectively, in the Ta_2NiSe_5 single crystal. The Knight shifts for Se3 correspond to the principal values of the Knight tensor, whereas the K_y data determined from the powder spectrum are also included for Se1 and Se2. The Knight shifts are anisotropic and dependent on the Se site. Except for K_c of Se3, the other Knight shifts gradually decrease with decreasing T in the orthorhombic phase, drop around T_c, and become constant toward $T = 0$ K. K_c of Se3 shows a different T dependence from the others due to the negative A_c^{hf}, as discussed below. The Knight shift values extrapolated to $T = 0$ K, K_α^0 ($\alpha = a^*, b, c$), are listed in Table II and presented by the horizontal lines in Fig. 5. Also the T dependence of the isotropic Knight shift $K_{iso} = (K_x + K_y + K_z)/3 = (K_a + K_b + K_c)/3$ for the Se1–Se3 sites is presented in Fig. 5(d). The Se2 site has almost

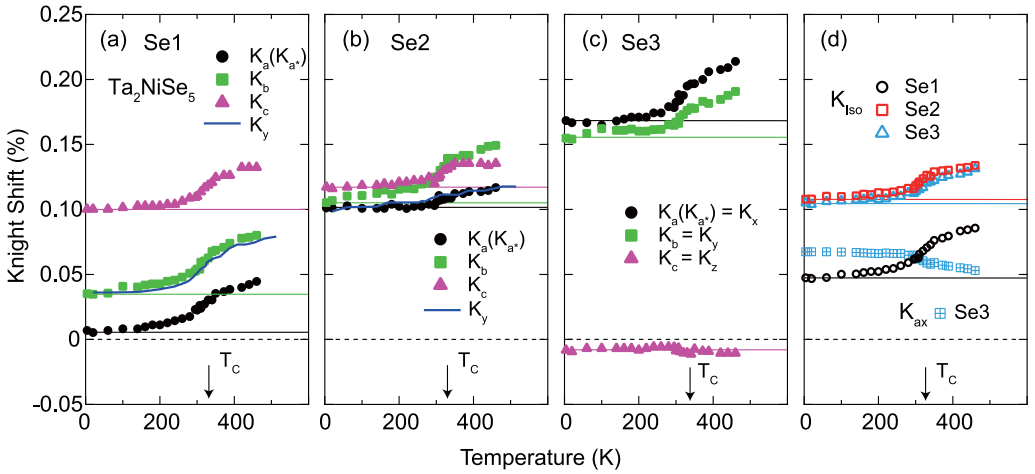

FIG. 5. Temperature dependences of the ^{77}Se Knight shifts, K_a (K_{a^*}), K_b, and K_c, for the (a) Se1, (b) Se2, and (c) Se3 sites in the single-crystalline Ta_2NiSe_5 sample. (d) Temperature dependences of the isotropic ^{77}Se Knight shift K_{iso} for the Se1, Se2, and Se3 sites and the axially anisotropic Knight shift K_{ax} for the Se3 site. The K_y data determined from the analysis of the powder spectrum are also presented for the Se1 and Se2 sites, whereas the Se3 Knight shifts correspond to the principal components. The solid lines represent the values extrapolated to $T = 0$ K.

the same K_{iso} as that of the Se3 site. The T dependence of the axially anisotropic Knight shift $K_{ax} = (2K_z - K_x - K_y)/6$ is also shown for Se3.

In general, the Knight shift scales with magnetic susceptibility. Figures 6(a), 6(b) and 6(c) show the K_α versus magnetic susceptibility χ plots for Se1, Se2, and Se3, respectively, whereas the K_{iso} versus χ plot is displayed in Fig. 6(d), which includes the K_{ax} versus χ plot for Se3. Here, we used χ data above 100 K after subtracting the impurity term from the powder susceptibility [18], as shown in the inset of Fig. 6(d). The Knight shifts scale with χ as $K_\alpha = A_\alpha^{hf}\chi/(N\mu_B) + C$ [$\alpha = a$ (a^*), b, c, iso, and ax], with C being a constant. The slopes of the straight lines, which are the results of fitting the data to the relation, provide the A_α^{hf} values listed in Table III.

C. Nuclear spin-lattice relaxation rate

The nuclear spin-lattice relaxation rate $1/T_1$ is useful for investigating dynamical magnetic properties. In general, $1/T_1T$ is proportional to $\Sigma_{\mathbf{q}}|A(\mathbf{q})|^2 \mathrm{Im}\chi_\perp(\mathbf{q},\omega_n)/\omega_n$, where $A(\mathbf{q})$ is the wave vector $\mathbf{q}$ component of the hyperfine coupling constant, $\mathrm{Im}\chi_\perp(\mathbf{q},\omega_n)$ is the imaginary part of the transverse dynamical susceptibility, and ω_n is the nuclear Larmor frequency [36].

Figure 7 shows the T dependences of $1/T_1$ for the Se1 and Se2 sites. The $1/T_1$ data were measured for the K_y singularity in the Se1 and Se2 powder NMR spectra (see Fig. 4), whereas the poor signal-to-noise ratio prevented us from precisely measuring $1/T_1$ for the single crystal. In the orthorhombic phase, $1/T_1$ gradually decreases with decreasing T and starts to rapidly drop at ~350 K. In the monoclinic phase, $1/T_1$ obeys the thermally activated T dependence $1/T_1 \propto \exp[-E_g/(k_BT)]$, with $E_g = 1770 \pm 40$ K for Se2 in the T range of 240 K $< T <$ T_c, as represented by the solid (dashed above T_c) curve and line in Figs. 7(a) and 7(b). However, below ~240 K, the nuclear magnetization decay changes from a single-exponential function to a stretched-exponential function, which is expressed as $P(t) = P(0)\exp[-(t/T_1)^{\beta_d}]$, with β_d being a constant. The inset in Fig. 7(b) shows the T dependence of the exponent β_d, which changes from unity to 0.5 with decreasing T below ~200 K. This stretched-exponential function comes from a magnetic impurity relaxation [37]. The deviation from the thermally activated behavior of $1/T_1$ at low temperatures is seen in Fig. 7(b), which displays the $1/T_1$ versus $1/T$ plot. This is reasonably ascribed to a magnetic impurity which provides the rapid increase in magnetic susceptibility at low temperatures. Thus, the intrinsic $1/T_1$ obeys the thermally activated T dependence with $E_g = 1770 \pm 40$ K, consistent with the excitation gap of $E_{op} \sim 0.16$ eV in the optical conductivity [23].

TABLE II. ^{77}Se Knight shifts extrapolated to $T = 0$ K, $K^0_{a^*}$, K^0_b, K^0_c, and K^0_{iso}, in the monoclinic phase of the single-crystalline Ta_2NiSe_5 sample.

Site	$K^0_{a^*}$ (%)	K^0_b (%)	K^0_c (%)	K^0_{iso} (%)
Se1	0.007	0.045	0.100	0.051
Se2	0.101	0.107	0.123	0.108
Se3	0.168	0.158	−0.009	0.105

IV. ANALYSIS AND DISCUSSION

A. Site symmetry and transferred hyperfine interaction

The NMR spectrum is sensitive to the site symmetry at each Se site. We discuss the hyperfine interaction governed by the site symmetry. In the monoclinic phase (space group $C2/c$), the Se3 site has a twofold rotation axis along the b axis, whereas the Se1 and Se2 sites have no site symmetry. These site symmetries and the β_m value close to 90° lead to the Se3 Knight shift tensor, which has approximately the a^*, b, and c axes as the principal axes, and the Se2 and Se3 tensors, for which those axes are not the principle axes. On the other hand, in the orthorhombic phase (space group $Cmcm$ [18]), the Se3 site with site symmetry $m2m$ is located on the two mirror planes perpendicular to the a and c axes, as presented in Fig. 1(b), leading to the principal a, b, and c axes of the K tensor. The Se1 and Se2

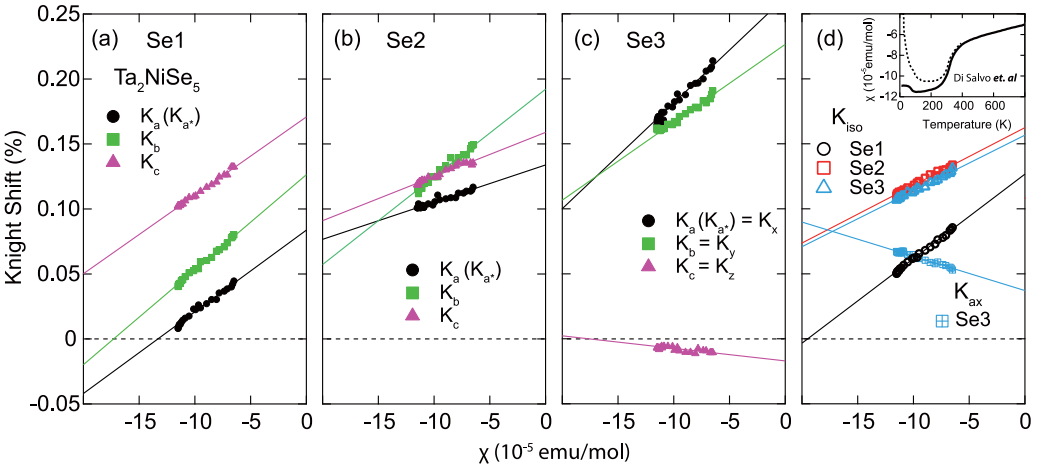

FIG. 6. ^{77}Se Knight shifts, K_a (K_{a^*}), K_b, and K_c, versus magnetic susceptibility χ plots for the (a) Se1, (b) Se2, and (c) Se3 sites in the single-crystalline Ta_2NiSe_5 sample. (d) ^{77}Se isotropic Knight shift K_{iso} versus χ plots for the Se1, Se2, and Se3 sites. The axially anisotropic ^{77}Se Knight shift K_{ax} versus χ for Se3 is also included in (d). The straight lines are the results of fitting the experimental data to the relation $K_\alpha = A_\alpha \chi/(N\mu_B) + C$ [$\alpha = a$ (a^*), b, c, iso, and ax], where A_α is the hyperfine coupling constant and C is a constant. The χ data (solid curve) above 100 K after subtracting the impurity term from the raw data (dashed curve) in Ref. [18] as displayed in the inset of (d) are utilized for the present plots. Also χ data are presented in units of emu per mole of Ta_2NiSe_5.

sites with site symmetry m.. are located only on the bc mirror plane, resulting in the principal a axis. Thus, the orthorhombic structure is consistent with the present NMR results.

Using the Knight shift tensors determined above, we discuss the microscopic interactions which govern them. The Sej (j = 1,2, and 3) site, a ligand site, may have a Knight shift tensor $\mathbf{K}$(Sej) expressed as

$$\mathbf{K}(\mathrm{Se}j) = \frac{1}{N\mu_B}[\mathbf{A}_{\mathrm{TH}}\boldsymbol{\chi}_{\mathrm{spin}} + \mathbf{A}_{\mathrm{orb}}\boldsymbol{\chi}_{\mathrm{orb}} + (\mathbf{A}_{\mathrm{dip}} + \mathbf{A}_{\mathrm{L}} + \mathbf{A}_{\mathrm{demag}})\boldsymbol{\chi}] + \mathbf{K}_{\mathrm{chem}}, \quad (2)$$

where N is Avogadro's number and μ_B is the Bohr magneton. $\mathbf{A}_{\mathrm{TH}}$ is the TH coupling tensor due to the spin susceptibility tensor $\boldsymbol{\chi}_{\mathrm{spin}}$. Note that the local spin susceptibility of the Ni site is assumed to be equal to that of the Ta site. $\mathbf{A}_{\mathrm{orb}}$ is the orbital hyperfine coupling tensor due to the orbital susceptibility tensor $\boldsymbol{\chi}_{\mathrm{orb}}$. $\mathbf{A}_{\mathrm{dip}}$ is the coupling tensor of the dipole field coming from the magnetic moments in a Lorentz sphere. Using the orthorhombic crystal structure [17], we can numerically calculate $\mathbf{A}_{\mathrm{dip}} = (0.16, 0.18, -0.34)\,\mathrm{kOe}/\mu_B$. $\mathbf{A}_{\mathrm{L}} = 4\pi\mu_B\mathbf{E}/(3v)$, with $\mathbf{E}$ being the unit matrix and v being the volume of a unit cell, is that of the Lorentz field, which is calculated as $A_{\mathrm{L}} = 0.24\,\mathrm{kOe}/\mu_B$. $\mathbf{A}_{\mathrm{demag}}$ is that of the demagnetization field, $\mathbf{A}_{\mathrm{demag}} = (A^{aa}_{\mathrm{demag}}, A^{bb}_{\mathrm{demag}}, A^{cc}_{\mathrm{demag}}) = (0, -4\pi\mu_B/v, 0) = (0, -0.71, 0)\,\mathrm{kOe}/\mu_B$ for Ta_2NiSe_5 with a sheet ac plane. $\boldsymbol{\chi}$ is the magnetic susceptibility tensor and $\mathbf{K}_{\mathrm{chem}}$ is the chemical shift tensor.

TABLE III. ^{77}Se hyperfine coupling constants A^{hf}_α [$\alpha = a$ (a^*), b, c, iso, and ax] for the Se1, Se2, and Se3 sites in the single-crystalline Ta_2NiSe_5 sample. The A_α values are presented in units of kOe/μ_B.

Site	A^{hf}_a ($A^{\mathrm{hf}}_{a^*}$)	A^{hf}_b	A^{hf}_c	$A^{\mathrm{hf}}_{\mathrm{iso}}$	$A^{\mathrm{hf}}_{\mathrm{ax}}$
Se1	35.1	40.8	33.7	36.5	
Se2	16.0	37.7	19.0	24.2	
Se3	45.4	33.4	−5.36	24.5	−14.7

In Ta_2NiSe_5, the Se1 site has one Ni and two Ta sites as its neighbors which contribute to the TH field, Se2 has three Ta sites, and Se3 has two Ni and two Ta sites, as seen in Fig. 1(b). Therefore, the TH coupling tensor of each Se site is expressed as

$$\mathbf{A}_{\mathrm{TH}}(\mathrm{Se1}) = \mathbf{A}^{(1)}(\mathrm{Se1}) + \sum_{i=1}^{2}\mathbf{B}^{(i)}(\mathrm{Se1}), \quad (3)$$

$$\mathbf{A}_{\mathrm{TH}}(\mathrm{Se2}) = \mathbf{A}^{(1)}(\mathrm{Se2}) + \sum_{i=1}^{2}\mathbf{B}^{(i)}(\mathrm{Se2}), \quad (4)$$

$$\mathbf{A}_{\mathrm{TH}}(\mathrm{Se3}) = \sum_{i=1}^{2}\mathbf{A}^{(i)}(\mathrm{Se3}) + \sum_{i=1}^{2}\mathbf{B}^{(i)}(\mathrm{Se3}), \quad (5)$$

where $\mathbf{A}^{(i)}$(Sej) and $\mathbf{B}^{(i)}$(Sej) are the TH coupling tensors due to the nearest-neighbor ith Ni and Ta ions of the Sej ion, respectively. In the orthorhombic phase, the site symmetry of the Se1–Se3 sites leads to the TH tensors expressed by Eqs. (A5)–(A7), respectively.

As seen in Eqs. (A5)–(A7), in the orthorhombic phase, the a axis is one of the principal axes, and the others are located on the bc plane for the Se1 and Se2 sites, whereas the a, b, and c axes are the principal axes for the Se3 site. Also the site symmetry requires the same anisotropy for the orbital and dipole terms. Thus, the expected anisotropy for the $\mathbf{K}$(Sej) tensor is consistent with the experimental results. We can conclude that $\mathbf{K}$(Sej) is governed from a microscopic point of view by the site symmetry and the local structure displayed in Fig. 1(b).

B. Local magnetic susceptibility

In general, magnetic susceptibility can be expressed as $\chi = \chi_{\mathrm{spin}}(T) + \chi_{\mathrm{orb}}(T) + \chi_{\mathrm{dia}}$, with $\chi_{\mathrm{spin}}(T)$ being the spin susceptibility, $\chi_{\mathrm{orb}}(T)$ being the orbital susceptibility, and χ_{dia}

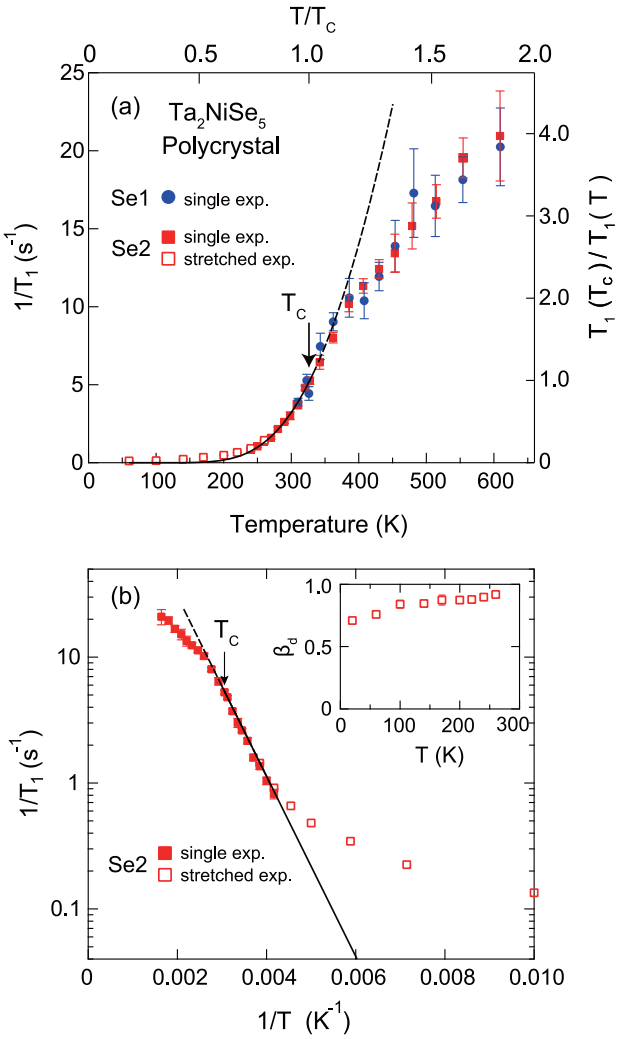

FIG. 7. (a) Temperature dependences of the ^{77}Se nuclear spin-lattice relaxation rate $1/T_1$ for the Se1 and Se2 sites in the polycrystalline Ta_2NiSe_5 sample. The solid and open symbols are the T_1 data in the single-exponential and stretched-exponential decays, respectively. The right and top axes refer to $T_1(T_c)/T_1(T)$ and T/T_c, respectively. (b) $1/T_1$ versus $1/T$ plot for the Se2 site in the polycrystalline Ta_2NiSe_5 sample. The inset shows the T dependence of β_d in the stretched exponential decay. The solid (dashed above T_c) curve and line represent the result of fitting the data to a thermally activated function with an energy gap of $E_g = 1770$ K.

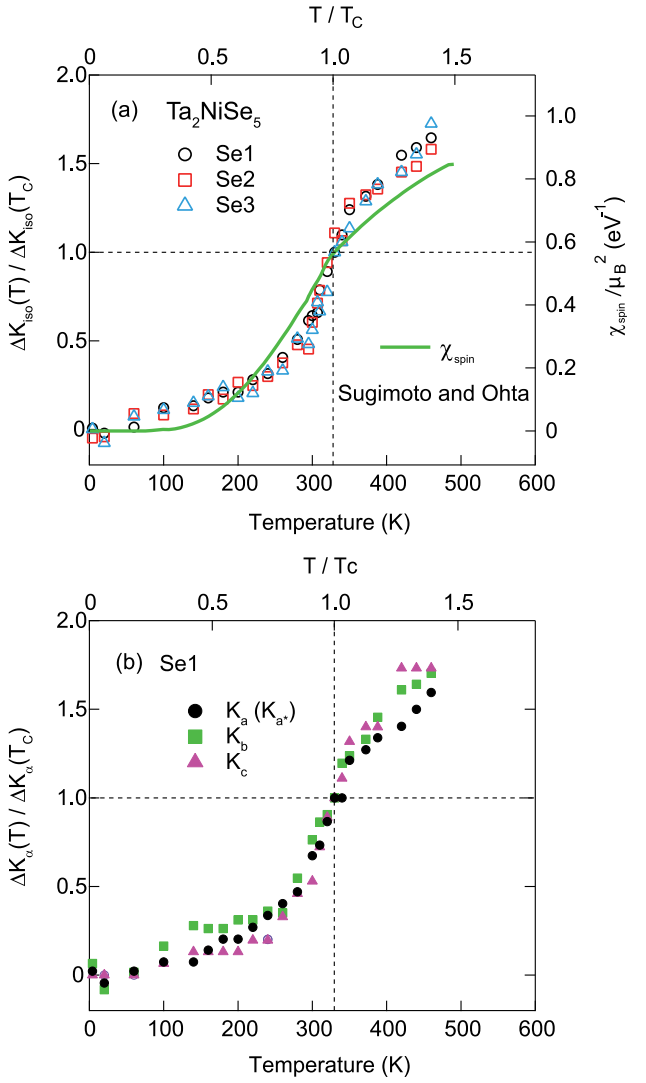

FIG. 8. Temperature dependences of (a) the normalized isotropic ^{77}Se Knight shifts $\Delta K_{iso}(T)/\Delta K_{iso}(T_c)$ for the Se1, Se2, and Se3 sites and (b) the normalized Knight shifts $\Delta K_\alpha(T)/\Delta K_\alpha(T_c)$ [$\alpha = a$ (a^*), b, c] for the Se1 site in Ta_2NiSe_5. $\Delta K_\alpha(T)$ is defined as $\Delta K_\alpha(T) = K_\alpha(T) - K_\alpha^0$ [$\alpha =$ iso, a (a^*), b, c]. The green curve represents the spin susceptibility calculated for the two-dimensional three-band model [30]. The top axis refers to the normalized temperature T/T_c.

being the T-independent core diamagnetic susceptibility. In Ta_2NiSe_5, χ_{dia} has the largest absolute value, as seen in the inset of Fig. 6(d). Regarding the aspect of the exciton condensation, note that $\chi_{spin}(T)$ and $\chi_{orb}(T)$ are able to monitor it via a change at T_c, as discussed in Refs. [30,31]. The modification of the band structure driven by the exciton condensation leads to the change in $\chi_{spin}(T)$, as discussed by Sugimoto and Ohta, who calculated the T dependence of $\chi_{spin}(T)$ presented in Fig. 8 within a mean-field approximation for the two-dimensional three-band model [30]. On the other hand, $\chi_{orb}(T)$ is shown to have two components, $\chi_{pp}(T)$, which is due to the coherent hopping between chains induced by the formation of the excitonic state, and $\chi_{t_2}(T)$, which is due to the correction of the transfer integral under a magnetic field, as discussed in the two-chain model by Matsuura and Ogata [31]. Then $\chi_{pp}(T)$ shows a T dependence different from that of $\chi_{t_2}(T)$. Sugimoto and Ohta also obtained a diamagnetic $\chi_{orb}(T)$ calculated within the two-dimensional three-band model in addition to $\chi_{spin}(T)$ [30]. Thus, it is meaningful to compare the calculated results with the Knight shift data which monitor the intrinsic magnetic susceptibility with no impurity contribution.

First, we discuss the Knight shift K_α^0 ($\alpha = a^*, b, c$) at $T = 0$ K. As seen in Table II, K_α^0 is anisotropic and Se site dependent. The K_α^0 data include information on $\chi_{orb}^\alpha(0)$ proportional to $K_{orb}^\alpha(0)$ because $K_\alpha^0 = K_{orb}^\alpha(0) + K_{chem}^\alpha$, where $K_{spin}^\alpha(0)$ becomes zero. However, unknown K_{chem}^α values prevent us from obtaining $K_{orb}^\alpha(0)$. Next, we concentrate our attention on the T-dependent part of $K(T)$ after subtracting K^0. Note that it is ascribed to both the T-dependent spin susceptibility

and the T-dependent part of the orbital susceptibility. Figure 8(a) shows the $\Delta K_{\rm iso}(T)/\Delta K_{\rm iso}(T_{\rm c})$ versus T plot, where $\Delta K_{\rm iso}(T) = K_{\rm iso}(T) - K^0_{\rm iso}$, for the Se1, Se2, and Se3 sites. The T dependences of $\Delta K_{\rm iso}(T)/\Delta K_{\rm iso}(T_{\rm c})$ for Se1, Se2, and Se3 scale with each other and change at $T_{\rm c}$, as seen in Fig. 8(a). We compare the experimental data with the spin susceptibility calculated for the two-dimensional three-band model [30]. In Fig. 8(a) the green curve is the paramagnetic $\chi_{\rm spin}$, which cannot reproduce the experimental data of $\Delta K_{\rm iso}(T)/\Delta K_{\rm iso}(T_{\rm c})$. Although the difference between $\chi_{\rm spin}$ and the experimental data is expected to come from $\chi_{\rm orb}$, the deviation cannot be explained well by the orbital susceptibility calculated for the three-band model [30] and the two-chain model [31]. The diamagnetic orbital susceptibility due to the exciton condensation $\chi_{\rm pp}$ is expected to be anisotropic and to appear for H_0 perpendicular to the b plane [31]. Figure 8(b) shows the T dependence of $\Delta K_\alpha(T)/\Delta K_\alpha(T_{\rm c})$ [$\alpha = a$ (a^*), b, c], where $\Delta K_\alpha(T) = K_\alpha(T) - K^0_\alpha$, for the Se1 site. The $\Delta K_b(T)$ data do not largely deviate in comparison with $\Delta K_{a^*}(T)$ and $\Delta K_c(T)$ below T_c, which means that $\chi_{\rm pp}$ may be small in Ta_2NiSe_5. Thus, more realistic calculations are necessary to quantitatively compare the ^{77}Se Knight shift with the spin and orbital susceptibilities based on the theoretical models in Ta_2NiSe_5 because the calculated magnetic susceptibilities are strongly parameter dependent.

C. Electron orbital polarization

$K_{\rm iso}$ may come from the isotropic TH interaction via the mixing between a Ni $3d$ (or Ta $5d$) orbital and a Se hybrid orbital composed of $4s$ and $4p$. We can obtain the fraction of the $4s$ orbital polarization f_{4s} by comparing the experimental values of $3A^{\rm hf}_{\rm iso}$ after correcting the isotropic coupling due to the Lorentz field $A_{\rm L} = 0.24\,{\rm kOe}/\mu_{\rm B}$ for the $A^{\rm hf}_{\rm iso}$ values listed in Table III with the Hartree-Fock value of the Se $4s$ orbital $A_{4s} = 8870\,{\rm kOe}/\mu_{\rm B}$ [38]. Here, χ is assumed to be expressed as $\chi = \chi({\rm Ni}) + 2\chi({\rm Ta})$ and $\chi({\rm Ni}) = \chi({\rm Ta})$, where $\chi({\rm Ni})$ and $\chi({\rm Ta})$ are magnetic susceptibilities in units of emu/Ni-mol and emu/Ta-mol, respectively. The result is that $f_{4s} = 1.23\%$, 0.81%, and 0.81% for the Se1, Se2, and Se3 sites, respectively. On the other hand, the anisotropic TH coupling constant provides information on the fraction of the Se $4p$ orbital polarization f_{4p}, perhaps via the mixing of Ni $3d$ and the Se hybrid orbital for the Se3 site. We obtain $f_{4p} = 24.0\%$ by comparing the experimental value of $3A^{\rm hf}_{\rm ax}$ after correcting the dipole coupling tensor $\mathbf{A}_{\rm dip}$ and the demagnetization one $\mathbf{A}_{\rm demag}$ numerically calculated in Sec. IV A for the $A^{\rm hf}_{\rm ax}$ value in Table III with the Hartree-Fock value of the $4p$ axially anisotropic hyperfine coupling constant, $A_{4p} = 183\,{\rm kOe}/\mu_{\rm B}$ [38]. The large f_{4p} value is consistent with the valence band composed of the Ni $3d$ and Se $4p$ orbitals shown by the ARPES measurements [15] and the first-principles calculation [20,21]. On the other hand, since the TH coupling tensors have off-diagonal components for Se1 and Se2, these complicated TH interactions prevent us from determining the TH coupling tensor of each Sej-Ni or Sej-Ta ($j = 1$ and 2) bond.

D. Magnetic excitation

As is well known, the BCS condensation of Cooper pairs takes place at a superconducting (SC) transition temperature. Then $1/T_1$ shows a coherence peak, whereas no coherence peak appears in the ultrasonic attenuation rate $\alpha_{\rm u}$ just below the SC transition temperature in BCS superconductors [39]. Similarly, the condensation of electron-hole pairs provides an effect on $1/T_1$ and $\alpha_{\rm u}$. For the simple two-band model, $1/T_1$ and $\alpha_{\rm u}$ are able to have a coherence peak just below $T_{\rm c}$ [40,41]. Recently, Sugimoto *et al.* calculated the T dependence of $1/T_1$ and $\alpha_{\rm u}$ in the BCS-type mean-field approximation for the three-chain Hubbard model with electron-phonon coupling [29]. This model has successfully explained the excitonic condensation and the structural transition from orthorhombic to monoclinic crystal structures at $T_{\rm c}$ in Ta_2NiSe_5 [19–22]. Sugimoto *et al.* found that no coherence peak appears just below $T_{\rm c}$ in $1/T_1$, in contrast to the result based on the simple two-band model, whereas a coherence peak appears in $\alpha_{\rm u}$. Thus, this is expected to provide a useful method to elucidate whether the exciton condensation takes place or not in Ta_2NiSe_5.

We could make the $1/T_1$ measurement as mentioned in Sec. III C, whereas the thin single crystal of Ta_2NiSe_5 prevented us from performing the ultrasonic measurement. As seen in Fig. 7, $1/T_1$ shows no coherence peak just below $T_{\rm c}$ and obeys the thermally activated T dependence with decreasing T. This is inconsistent with the behavior of $1/T_1$ calculated for the simple two-band model [40]. Although the damping of the coherence peak may be expected from impurity effects [42], this model is too simple to describe the exciton condensation in Ta_2NiSe_5. On the other hand, the present $1/T_1$ result is consistent with the theoretical prediction by Sugimoto *et al.* [29]. The thermally activated T dependence of $1/T_1$ remains up to about 380 K, as seen in Fig. 7 (b). This is observed by the ARPES experiment in which the flat-top valence band remains above $T_{\rm c}$ [22]. This is also reproduced by the calculation in the finite-temperature variational cluster approximation and is concluded to be due to the exciton fluctuation.

V. CONCLUSION

We conducted ^{77}Se NMR measurements on polycrystalline and single-crystalline samples to elucidate the local electronic state in a candidate for the excitonic insulator, Ta_2NiSe_5. The Knight shift tensors of the three Se sites were determined in the monoclinic and orthorhombic phases, which is consistent with the site symmetry and the local configuration of the neighboring Ni and Ta sites. Based on the temperature dependence of the Knight shifts, we discussed the reduction in spin and orbital susceptibilities due to the formation of the exciton condensation. We also estimated the polarization fraction values of the Se $4s$ and Se $4p$ orbitals from the hyperfine coupling constants. The nuclear spin-lattice relaxation rate $1/T_1$ was found not to show a coherence peak just below $T_{\rm c}$, which is considered to result from the excitonic condensation as predicted by the $1/T_1$ calculation in the BCS-type mean-field approximation. Also, below $T_{\rm c}$, $1/T_1$ showed spin-gap behavior with an energy gap of $E_{\rm g} = 1770 \pm 40$ K. Thus, we concluded that NMR is a useful probe to detect the exciton condensation in excitonic insulators.

ACKNOWLEDGMENTS

The authors would like to thank K. Sugimoto, Y. Ohta, H. Matsuura, A. Kobayashi, and Y. Suzumura for fruitful

discussions and S. Inoue for technical support. This study was supported by KAKENHI (Grants No. 24340080 and No. 16K13835) from the Japan Society for the Promotion of Science (JSPS). S.L. would like to thank the Program for Leading Graduate Schools entitled "PhD professional: Gateway to Success in Frontier Asia."

APPENDIX: TRANSFERRED HYPERFINE COUPLING TENSOR BASED ON THE SE SITE SYMMETRY

We present the transferred hyperfine (TH) coupling tensor for each Se site in the orthorhombic phase (space group $Cmcm$) of Ta_2NiSe_5 based on the site symmetry. The anisotropy of the Knight shift tensor is mainly governed by the configuration of the neighboring nickel and tantalum sites of the Se site. The Se1 site is located on a mirror plane perpendicular to the a axis, as shown in Fig. 1(b). If we express the TH tensor from one Ni site to the Se1 site as

$$\mathbf{A}^{(1)}(\mathrm{Se1}) = \begin{pmatrix} A^{(1)}_{aa}(\mathrm{Se1}) & A^{(1)}_{ab}(\mathrm{Se1}) & A^{(1)}_{ac}(\mathrm{Se1}) \\ A^{(1)}_{ba}(\mathrm{Se1}) & A^{(1)}_{bb}(\mathrm{Se1}) & A^{(1)}_{bc}(\mathrm{Se1}) \\ A^{(1)}_{ca}(\mathrm{Se1}) & A^{(1)}_{cb}(\mathrm{Se1}) & A^{(1)}_{cc}(\mathrm{Se1}) \end{pmatrix}, \quad \text{(A1)}$$

it satisfies $\mathbf{A}^{(1)}(\mathrm{Se1}) = \boldsymbol{\sigma}_a \mathbf{A}^{(1)}(\mathrm{Se1}) \boldsymbol{\sigma}_a^{-1}$, where $\boldsymbol{\sigma}_a$ is the symmetry operation tensor through the mirror plane perpendicular to the a axis, because the Ni site itself is on the mirror plane. Thus, we have

$$\mathbf{A}^{(1)}(\mathrm{Se1}) = \begin{pmatrix} A^{(1)}_{aa}(\mathrm{Se1}) & 0 & 0 \\ 0 & A^{(1)}_{bb}(\mathrm{Se1}) & A^{(1)}_{bc}(\mathrm{Se1}) \\ 0 & A^{(1)}_{cb}(\mathrm{Se1}) & A^{(1)}_{cc}(\mathrm{Se1}) \end{pmatrix}. \quad \text{(A2)}$$

On the other hand, if we express the TH tensor from one of the two Ta sites to the Se1 site as

$$\mathbf{B}^{(1)}(\mathrm{Se1}) = \begin{pmatrix} B^{(1)}_{aa}(\mathrm{Se1}) & B^{(1)}_{ab}(\mathrm{Se1}) & B^{(1)}_{ac}(\mathrm{Se1}) \\ B^{(1)}_{ba}(\mathrm{Se1}) & B^{(1)}_{bb}(\mathrm{Se1}) & B^{(1)}_{bc}(\mathrm{Se1}) \\ B^{(1)}_{ca}(\mathrm{Se1}) & B^{(1)}_{cb}(\mathrm{Se1}) & B^{(1)}_{cc}(\mathrm{Se1}) \end{pmatrix}, \quad \text{(A3)}$$

the TH tensor from another Ta site follows $\mathbf{B}^{(2)}(\mathrm{Se1}) = \boldsymbol{\sigma}_a \mathbf{B}^{(1)}(\mathrm{Se1}) \boldsymbol{\sigma}_a^{-1}$, resulting in

$$\mathbf{B}^{(2)}(\mathrm{Se1}) = \begin{pmatrix} B^{(1)}_{aa}(\mathrm{Se1}) & -B^{(1)}_{ab}(\mathrm{Se1}) & -B^{(1)}_{ac}(\mathrm{Se1}) \\ -B^{(1)}_{ba}(\mathrm{Se1}) & B^{(1)}_{bb}(\mathrm{Se1}) & B^{(1)}_{bc}(\mathrm{Se1}) \\ -B^{(1)}_{ca}(\mathrm{Se1}) & B^{(1)}_{cb}(\mathrm{Se1}) & B^{(1)}_{cc}(\mathrm{Se1}) \end{pmatrix}. \quad \text{(A4)}$$

Thus, the TH coupling of Se1 $\mathbf{A}_{\mathrm{TH}}(\mathrm{Se1})$ which comes from one Ni and Two Ta sites can be expressed as

$$\mathbf{A}_{\mathrm{TH}}(\mathrm{Se1}) = \begin{pmatrix} A^{(1)}_{aa}(\mathrm{Se1}) + 2B^{(1)}_{aa}(\mathrm{Se1}) & 0 & 0 \\ 0 & A^{(1)}_{bb}(\mathrm{Se1}) + 2B^{(1)}_{bb}(\mathrm{Se1}) & A^{(1)}_{bc}(\mathrm{Se1}) + 2B^{(1)}_{bc}(\mathrm{Se1}) \\ 0 & A^{(1)}_{cb}(\mathrm{Se1}) + 2B^{(1)}_{cb}(\mathrm{Se1}) & A^{(1)}_{cc}(\mathrm{Se1}) + 2B^{(1)}_{cc}(\mathrm{Se1}) \end{pmatrix}. \quad \text{(A5)}$$

We similarly obtain $\mathbf{A}_{\mathrm{TH}}(\mathrm{Se2})$ for the Se2 site on a mirror plane perpendicular to the a axis and $\mathbf{A}_{\mathrm{TH}}(\mathrm{Se3})$ for the Se3 site on two mirror planes perpendicular to the a and c axes, which are respectively expressed as

$$\mathbf{A}_{\mathrm{TH}}(\mathrm{Se2}) = \begin{pmatrix} B^{(1)}_{aa}(\mathrm{Se2}) + 2B^{(2)}_{aa}(\mathrm{Se2}) & 0 & 0 \\ 0 & B^{(1)}_{bb}(\mathrm{Se2}) + 2B^{(2)}_{bb}(\mathrm{Se2}) & B^{(1)}_{bc}(\mathrm{Se2}) + 2B^{(2)}_{bc}(\mathrm{Se2}) \\ 0 & B^{(1)}_{cb}(\mathrm{Se2}) + 2B^{(2)}_{cb}(\mathrm{Se2}) & B^{(1)}_{cc}(\mathrm{Se2}) + 2B^{(2)}_{cc}(\mathrm{Se2}) \end{pmatrix}, \quad \text{(A6)}$$

$$\mathbf{A}_{\mathrm{TH}}(\mathrm{Se3}) = 2\begin{pmatrix} A^{(1)}_{aa}(\mathrm{Se3}) + B^{(1)}_{aa}(\mathrm{Se3}) & 0 & 0 \\ 0 & A^{(1)}_{bb}(\mathrm{Se3}) + B^{(1)}_{bb}(\mathrm{Se3}) & 0 \\ 0 & 0 & A^{(1)}_{cc}(\mathrm{Se3}) + B^{(1)}_{cc}(\mathrm{Se3}) \end{pmatrix}. \quad \text{(A7)}$$

[1] B. I. Halperin and T. M. Rice, Rev. Mod. Phys. **40**, 755 (1968).
[2] F. X. Bronold and H. Fehske, Phys. Rev. B **74**, 165107 (2006).
[3] D. Ihle, M. Pfafferott, E. Burovski, F. X. Bronold, and H. Fehske, Phys. Rev. B **78**, 193103 (2008).
[4] K. Seki, R. Eder, and Y. Ohta, Phys. Rev. B **84**, 245106 (2011).
[5] B. Zenker, D. Ihle, F. X. Bronold, and H. Fehske, Phys. Rev. B **85**, 121102(R) (2012).
[6] P. Wachter, B. Bucher, and J. Malar, Phys. Rev. B **69**, 094502 (2004).
[7] B. Bucher, P. Steiner, and P. Wachter, Phys. Rev. Lett. **67**, 2717 (1991).
[8] P. Wachter, Solid State Commun. **118**, 645 (2001).
[9] D. P. Young, D. Hall, M. E. Torelli, Z. Fisk, J. L. Sarrao, J. D. Thompson, H.-R. Ott, S. B. Oseroff, R. G. Goodrich, and R. Zysler, Nature (London) **397**, 412 (1999).
[10] M. E. Zhitomirsky, T. M. Rice, and V. I. Anisimov, Nature (London) **402**, 251 (1999).
[11] E. Bascones, A. A. Burkov, and A. H. MacDonald, Phys. Rev. Lett. **89**, 086401 (2002).
[12] H. Cercellier, C. Monney, F. Clerc, C. Battaglia, L. Despont, M. G. Garnier, H. Beck, P. Aebi, L. Patthey, H. Berger, and L. Forró, Phys. Rev. Lett. **99**, 146403 (2007).
[13] J. van Wezel, P. Nahai-Williamson, and S. S. Saxena, Phys. Rev. B **81**, 165109 (2010).
[14] C. Monney, C. Battaglia, H. Cercellier, P. Aebi, and H. Beck, Phys. Rev. Lett. **106**, 106404 (2011).

[15] Y. Wakisaka, T. Sudayama, K. Takubo, T. Mizokawa, M. Arita, H. Namatame, M. Taniguchi, N. Katayama, M. Nohara, and H. Takagi, Phys. Rev. Lett. **103**, 026402 (2009).
[16] Y. Wakisaka, T. Sudayama, K. Takubo, T. Mizokawa, N. L. Saini, M. Arita, H. Namatame, M. Taniguchi, N. Katayama, M. Nohara, and H. Takagi, J. Supercond. Novel Magn. **25**, 1231 (2012).
[17] S. A. Sunshine and J. A. Ibers, Inorg. Chem. **24**, 3611 (1985).
[18] F. J. Di Salvo, C. H. Chen, R. M. Fleming, J. V. Waszczak, R. G. Dunn, S. A. Sunshine, and J. A. Ibers, J. Less-Common Met. **116**, 51 (1986).
[19] T. Kaneko, T. Toriyama, T. Konishi, and Y. Ohta, J. Phys.: Conf. Ser. **400**, 032035 (2012).
[20] T. Kaneko, K. Seki, and Y. Ohta, Phys. Rev. B **85**, 165135 (2012).
[21] T. Kaneko, T. Toriyama, T. Konishi, and Y. Ohta, Phys. Rev. B **87**, 035121 (2013).
[22] K. Seki, Y. Wakisaka, T. Kaneko, T. Toriyama, T. Konishi, T. Sudayama, N. L. Saini, M. Arita, H. Namatame, M. Taniguchi, N. Katayama, M. Nohara, H. Takagi, T. Mizokawa, and Y. Ohta, Phys. Rev. B **90**, 155116 (2014).
[23] Y. F. Lu, H. Kono, T. I. Larkin, A. W. Rost, T. Takayama, A. V. Boris, B. Keimer, and H. Takagi, Nat. Commun. **8**, 14408 (2017).
[24] A. Nakano, K. Sugawara, S. Tamura, N. Katayama, K. Matsubayashi, T. Okada, Y. Uwatoko, K. Munakata, A. Nakao, H. Sagayama, R. Kumai, K. Sugimoto, N. Maejima, A. Machida, T. Watanuki, and H. Sawa, IUCrJ. **5**, 158 (2018).
[25] S. Mor, M. Herzog, D. Golež, P. Werner, M. Eckstein, N. Katayama, M. Nohara, H. Takagi, T. Mizokawa, C. Monney, and J. Stähler, Phys. Rev. Lett. **119**, 086401 (2017).
[26] T. I. Larkin, A. N. Yaresko, D. Pröpper, K. A. Kikoin, Y. F. Lu, T. Takayama, Y.-L. Mathis, A. W. Rost, H. Takagi, B. Keimer, and A. V. Boris, Phys. Rev. B **95**, 195144 (2017).
[27] Y. Seo, M. J. Eom, J. S. Kim, C. Kang, B. I. Min, and J. Hwang, arXiv:1707.07839.
[28] S. Y. Kim, Y. Kim, C.-J. Kang, E.-S. An, H. K. Kim, M. J. Eom, M. Lee, C. Park, T.-H. Kim, H. C. Choi, B. I. Min, and J. S. Kim, ACS Nano **10**, 8888 (2016).
[29] K. Sugimoto, T. Kaneko, and Y. Ohta, Phys. Rev. B **93**, 041105(R) (2016).
[30] K. Sugimoto and Y. Ohta, Phys. Rev. B **94**, 085111 (2016).
[31] H. Matsuura and M. Ogata, J. Phys. Soc. Jpn. **85**, 093701 (2016).
[32] T. Yamada, K. Domon, and Y. Ōno, J. Phys. Soc. Jpn. **85**, 053703 (2016).
[33] K. Domon, T. Yamada, and Y. Ōno, arXiv:1705.05794.
[34] T. Suzuki, I. Yamauchi, M. Itoh, T. Yamauchi, and Y. Ueda, Phys. Rev. B **73**, 224421 (2006).
[35] M. Itoh, I. Yamauchi, T. Kozuka, T. Suzuki, T. Yamauchi, J. I. Yamaura, and Y. Ueda, Phys. Rev. B **74**, 054434 (2006).
[36] T. Moriya, J. Phys. Soc. Jpn. **18**, 516 (1963).
[37] M. Itoh, H. Yasuoka, A. R. King, and V. Jaccarino, J. Phys. Soc. Jpn. **55**, 964 (1986).
[38] A. K. Koh and D. J. Miller, At. Data Nucl. Data Tables **33**, 235 (1985).
[39] P. G. de Gennes, *Superconductivity of Metals and Alloys* (Benjamin, New York, 1966).
[40] K. Maki and N. Urata, J. Low Temp. Phys. **10**, 59 (1973).
[41] K. Maki and K. Nakanishi, J. Low Temp. Phys. **5**, 55 (1971).
[42] J. Zittartz, Phys. Rev. **164**, 575 (1967).